Available online at www.sciencedirect.com

jmr&t Journal of Materials Research and Technology

journal homepage: www.elsevier.com/locate/jmrt

Effects of skew rolling piercing process friction coefficient on tube twisting, strain rate and forming velocity

Hamed Aghajani Derazkola[*], *Eduardo Garcia*, *Alberto Murillo-Marrodán*

Department of Mechanics, Design and Industrial Management, University of Deusto, 48007 Bilbao, Spain

ARTICLE INFO

Article history:
Received 27 May 2023
Accepted 19 July 2023
Available online 22 July 2023

Keywords:
Skew rolling piercing
Friction coefficient
Finite element method
Super-martensitic Cr13 stainless steel
Plastic deformation

ABSTRACT

In this paper the effects of rollers-billet friction coefficient (RFC) and plug-billet friction coefficient (PFC) during the skew rolling piercing process are investigated. The piercing process has been simulated and the plastic deformation, temperature evolution, and surface twisting of pierced tube analysed. Results show that the plastic deformation of super-martensitic Cr13 stainless steel increases at higher RFC and decreases at higher PFC. The same trend has been observed for material strain rate, which increases with higher RFC but decreases with increasing PFC. In addition, it has been found that friction coefficient does not affect the temperature evolution of the billet. In fact, the material heating during piercing is related to plastic deformation. Comparison of the fracture surfaces of the hot tension test samples at 0.01 s^{-1} and 10 s^{-1} confirm this point. The RFC increases the forward material velocity, and PFC decreases the forward material during the skew rolling piercing process. The PFC decreases the material velocity due to the ductile fracture growth obstacle inside the tube. More plastic deformation at higher PFC leads to higher surface twisting. The maximum surface twisting was 68° at RFC = 0.6 and PFC = 0.06, and the minimum surface twisting was 12° at RFC = 0.2 and PFC = 0.15.

1. Introduction

During the production of seamless tubes in a factory, the skew rolling piercing phase is an early stage that creates an inner cavity in a cylindrical (bar) shape [1]. Before this piercing, the billet is heated up in a furnace, and the hot billet is transferred into the piercing setup. The working temperature is usually higher than 70% of the billet melting temperature. For this reason, this process is categorized as a hot deformation process. In this phase, a push bench moves the hot billet forward, and two big rollers push the hot billet forward. Between two rollers, a piercing plug start to pierce and stretch the billet all along its length [2]. At the same time, two big disks, called Dieschers, control the geometry of pierced billet to increase geometrical accuracy [3]. The piercing phase of seamless tube production is very short, which makes this process extremely complicated [4]. Ultra-high strain rate at high temperature puts the billet in extreme condition. Understanding thermo-mechanical phenomena to find the best process parameters is very difficult and expensive [5]. Finding optimum process parameters would be the most critical point to increase the tooling system working life and minimizing energy consumption in this process [6]. Simulation of the skew rolling

* Corresponding author.
E-mail address: h.aghajani@deusto.es (H.A. Derazkola).
https://doi.org/10.1016/j.jmrt.2023.07.167

piercing process can help researchers to understand the thermo-mechanical phenomena related to raw material (billet) behavior. The material (billet) behavior can affect the final product quality and working life of the tooling system. Urbański and Kazanecki [7] were early researchers that used the two-dimensional (2D) FEM method for piercing process simulation. They modeled the process by axially-symmetric state of strain to monitor the strain changes in the longitudinal direction of the tube. Mori et al. [8] analyzed the piercing phase using the 2D-FEM method and considered the process as a plane state of strain without friction contact between the billet and piercing plug contact surface. Mori [9], developed a model by considering the influence of friction on the billet-piercing plug interface. Ceretti et al. [10] applied the billet material model to predict cracks during the piercing process. They used the maximum tensile stress criterion to predict AISI1020 grade steel crack formation using the 2D-FEM method. They did not consider plug piercing in their simulation domain. The early attempts at a three-dimensional (3D) piercing process was not a comprehensive model with various details. Pietsch and Thieven [11] used a 3D-FEM model to simulate the process. They presented the stress and strain distribution in the longitudinal section of the pierced tube. In their simulation, the thermal aspects of the process were neglected. The same approach was used for the plug positioning during the piercing process by Ceretti et al. [12]. Berazategui et al. [13] simplified the piercing phase process simulation with the FEM method and compared the simulation results with experimental test. For the first time, Pater et al. [14] modeled all parts of the piercing phase, including rollers, Diescher disks, and plug, and included the heat phenomena in their model. After that, an analysis of the load of the piercing plug was developed by Pater and Kazanecki [15]. Pater et al. [14] developed a model to calculate temperature changes and distribution of surface pressure on the surface of the piercing plug. Zhao [16], studied the effects of rollers feed angles on the piercing process by the FEM method. The output results revealed that with increasing rollers feed angles, the rolling process's effectiveness increased, but the product quality decreased. Murillo-Marrodan et al. [17] analysed the effect of various friction models at the interfaces of tools and billet using a 3D FEM model. They used mainly Coulomb, Tresca, and viscoplastic friction models. They stated that the Tresca and viscoplastic models provide conditions similar to actual experimental tests. Fernandes et al. [18] investigated the effects of friction coefficient (at the tools–billet interface) on the stress and strain state using the 3D FEM method. They used the Tresca friction model at interfaces. They showed that the friction coefficient directly impacts billet feed efficiency, tube twist angle, and piercing plug force. The feed efficiency is defined as a ratio that shows the roll's capacity to push the billet forward. This ratio is introduced as a parameter that is related to the axial speed of Rolls. Aghajani Derazkola et al. [19] investigated the effects of friction coefficient on energy consumption during the piercing process. They optimized the friction coefficient at the interface of tools and billet to minimize energy consumption during the piercing process.

The main key factor in the skew rolling piercing process is the relation between physical phenomena during actual processes and simulation processes. The available literature shows that simulation of material behavior during the piercing process is very hard due to the complexity of the process. A billet is ruptured, twisted, and elongated simultaneously to obtain a seamless tube. During this process, friction plays a critical role in producing a sound tube. As mentioned earlier, this process involves high strain rates, since the billet is transformed quickly into the tube. For this reason, various metallurgical phenomena cannot be analyzed in a real production line. In this regard, material behavior analysis is necessary to describe seamless tube production. This article combines the material behavior results of super-martensitic Cr13 stainless steel hot tensile test with the 3D FEM simulation of the skew rolling piercing process to describe the thermo-mechanical phenomena during the actual seamless tube production process.

2. Experimental procedure

2.1. Raw material

In this study, super-martensitic Cr13 stainless steel is used as raw material. The raw material was provided by Tubos Reunidos [20] and was used for material behavior testing procedure and seamless tube process. The chemical composition of super-martensitic Cr13 stainless steel tested is presented in Table 1.

2.2. Hot tensile test

To compare the effects of strain rate on microstructure and fracture properties of super-martensitic Cr13 stainless steel, a hot tensile test was carried out. The testing temperature was 1100 °C, with 0.01 s^{-1}, 0.1 s^{-1}, 1 s^{-1}, and 10 s^{-1} strain rates. With various trial and error tests and with the help of simulation results detailed in the next section, it can be found that the raw billet (with 1250 °C) had a heat transfer with the piercing process tooling system. The internal temperature of the hot billet diminished to 1100 °C. For this reason, the hot tensile test was carried out at 1100 °C to reproduce the fracture process at the plug's tip. In this case, the plug starts to rupture internally of hot material at 1100 °C. The tensile sample was prepared according to the standard ASTM E21-09 (2020). The hot tensile test samples were put in cold water (~0 °C) immediately after the test to freeze the microstructure changes and prevent the fracture surface of samples from oxidation. Fig. 1a and b depicted pictures of the hot tensile test machine and tensile sample.

Table 1 – Chemical composition of super-martensitic Cr13 stainless steel.

Element	C	Cr	Ni	Mn	Si	Mo	P	S	Ti	V	Fe
Wt.%	0.03	11.5–13.5	4.5–6.5	0.5	0.5	1.5–3	0.03	0.005	0.01–0.5	0.5	Bal

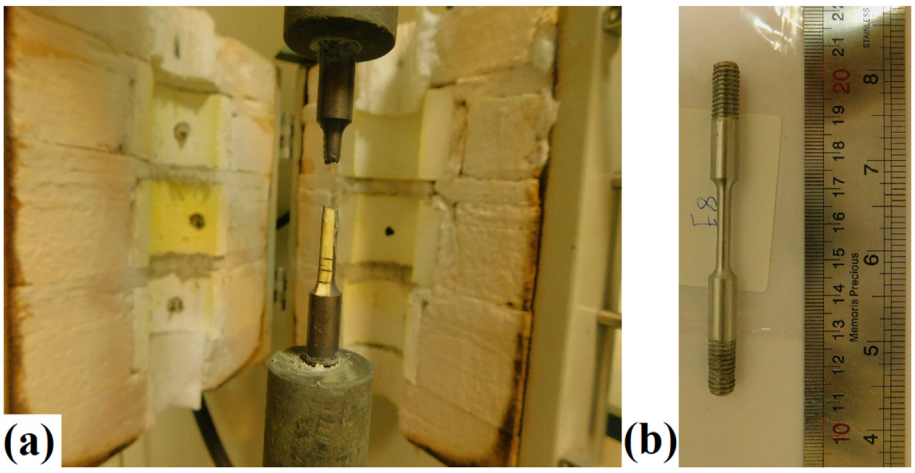

Fig. 1 – (a) Image of hot tensile test setup, (b) image of hot tensile test sample.

2.3. *Sample evaluations*

The fracture surface of the hot tensile test sample was evaluated by scanning electron microscopy (SEM) equipped with Energy-dispersive X-ray (EDS). Microstructure of hot tensile samples was evaluated by optical microscope (OM). For better analysis of the effect of the piercing process on the microstructure changes, the hot tensile test carried out, and the samples were put in cold water immediately after the test was finished—accordingly, the tensile test was cut, and evaluated by optical microscopy. Grain size is typically measured and classified using standardized methods. In this research, the ASTM E112 standard has been used for super-martensitic Cr13 stainless steel.

2.4. *Tube piercing process*

The industrial piercing process of the cylindrical bar of super-martensitic Cr13 stainless steel is described hereafter. In this research, the experimental part of tube piercing was carried out by Tubos Reunidos. In this study, two rollers piercing mill has been used.

It means that two rollers placed up and down of tube and two disks (Dieschers) placed on the sides of the tube are the responsible for guiding the billet through the process, while a plug placed in the center created the tube piercing [20]. The billet material was super-martensitic Cr13 stainless steel with a cylindrical shape of 202 mm diameter and 600 mm length. The raw material (billet) was heated up from room temperature to 1250 °C in a furnace. Then, the hot billet is moved from the furnace to the piercing process chamber with a guide of 208 mm. A thrust bench pushes the billet into the piercing mill at 100 mm/s traverse velocity. Two rollers push the hot billet forward (against the plug) by friction. Fig. 2a and b shows the piercing process tooling system and produced tube after piercing. The plug is fixed at the system's center and can freely rotate on its axis. For increasing friction between tools and piercing tube, the roller and plug surfaces are machined or hatched. The upper and lower rollers had the same geometry with 900 mm diameter with 1.5° profile angle, 0° cross angle, and 12° feed angle, respectively. The rollers were mirrored according to the middle of the super-martensitic Cr13 stainless steel billet. During the piercing process, the rollers had 111 rpm angular velocity. A schematic view of the piercing process is depicted in Fig. 2c.

3. Piercing process modelling

For this study a 3D FEM of the above described piercing process has been developed. Tool dimensions and locations were designed according to the experimental procedure. The billet material was selected as super-martensitic Cr13 stainless steel with Hansel-Spittel constitutive law:

$$\sigma = Ae^{m_1 T} T^{m_9} \varepsilon^{m_2} e^{\frac{m_4}{\varepsilon}} (1+\varepsilon)^{m_5 T} e^{m_7 \varepsilon} \dot{\varepsilon}^{m_3} \dot{\varepsilon}^{m_8 T} \quad (1)$$

In Equation (1), A, m_1, m_2, m_3, m_4, m_5, m_6, m_7 and m_8 are super-martensitic Cr13 stainless steel constant, T is temperature, ε and $\dot{\varepsilon}$ are presents the strain and strain rate.

The material flow behaviour was provided by Tubos Reunidos laboratory. With this model, the raw material behavior can be predictable at various temperatures and strain rates. A sample of super-martensitic Cr13 stainless steel flow stress at various temperature with 0.05 s^{-1} and 10 s^{-1} strain rates are presented in Fig. 3a and b, respectively.

3.1. *Contact and friction model*

This study considered smooth contact without friction for the thrust bench and guide contact surfaces with billet. The friction is considered in the interface of rollers, plug, and Dieschers with billet. The viscoplastic friction model is considered for rollers and billet interfaces:

$$\tau = \alpha K \left(\sqrt{\|V_{rel}\|^2 + v_{reg}^2} \right)^{(pf-1)} V_{rel} \quad (2)$$

where α is the viscoplastic friction coefficient ($0 < \alpha < 1$), whose value is dependent on the normal stress, K is the material

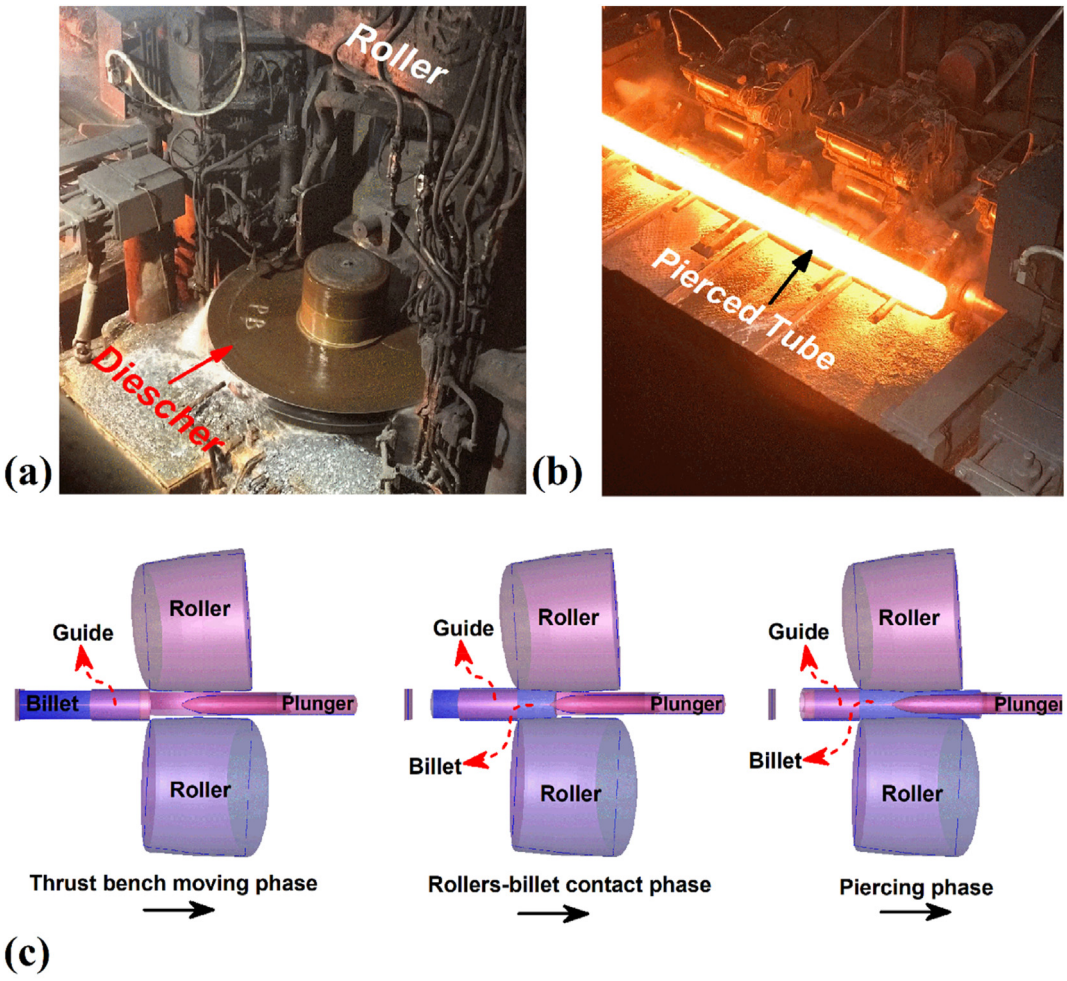

Fig. 2 – (a) Heating up of billet, (b) Pierced tube. (c) Schematic view of skew rolling piercing process.

consistency and pf the sensitivity to sliding velocity, with a value similar to the strain rate sensitivity index of the rheological model. V_{rel} is relative velocity, and the v_{reg} is regularisation velocity. In this model the Roller-billet interface is consider as a viscoplastic layer. The Tresca friction model is considered for plug and Dieschers interfaces that were in contact with billet:

$$\tau = mk\frac{V_{rel}}{\sqrt{|V_{rel}|^2 + v_{reg}^2}} \quad (3)$$

The Tresca friction model is used when shear stress (τ) exceeds the shear strength (k) of the raw material. In the Tresca friction model, the coefficient (m) stands for the friction factor, and its value ranges between $0 < m < 1$. Due to higher contact friction and high rotational velocity at the Roller-billet interface, the viscoplastic friction model was selected for this area. For other regions, the Tresca friction model was selected. In this model the Roller-billet interface is consider as a shear layer. The more details of the friction model selection are described in previous research published by authors [19].

This study selects a friction coefficient range for rollers and plug interfaces with the billet. These ranges are selected according to the producibility of the tube and optimum energy consumption during the process [19]. These ranges were selected after arranging by the physical phenomenon collected from the actual process. The friction coefficient at the rollers and billet interface (RFC) is between 0.1 and 0.6, and the friction coefficient at the plug and billet interface (PFC) is between 0.06 and 0.15. Table 2 summarizes the friction coefficients considered in this study.

3.2. *Finite element model*

This process is simulated by the finite element method (FEM) using the commercial software FORGE® NX (Version 3.2). This software is specifically developed for hot and cold metal forming processes. For the heating phase, the billet temperature is increased up to 1250 °C; the thrust bunch is pushed forward the billet for the piercing process. The tool system kinematics are selected according to the experimental test.

The billet is defined as a deformable object, using the constitutive model Hansel-Spittel above described, and the tooling system is a rigid body with thermal conductivity

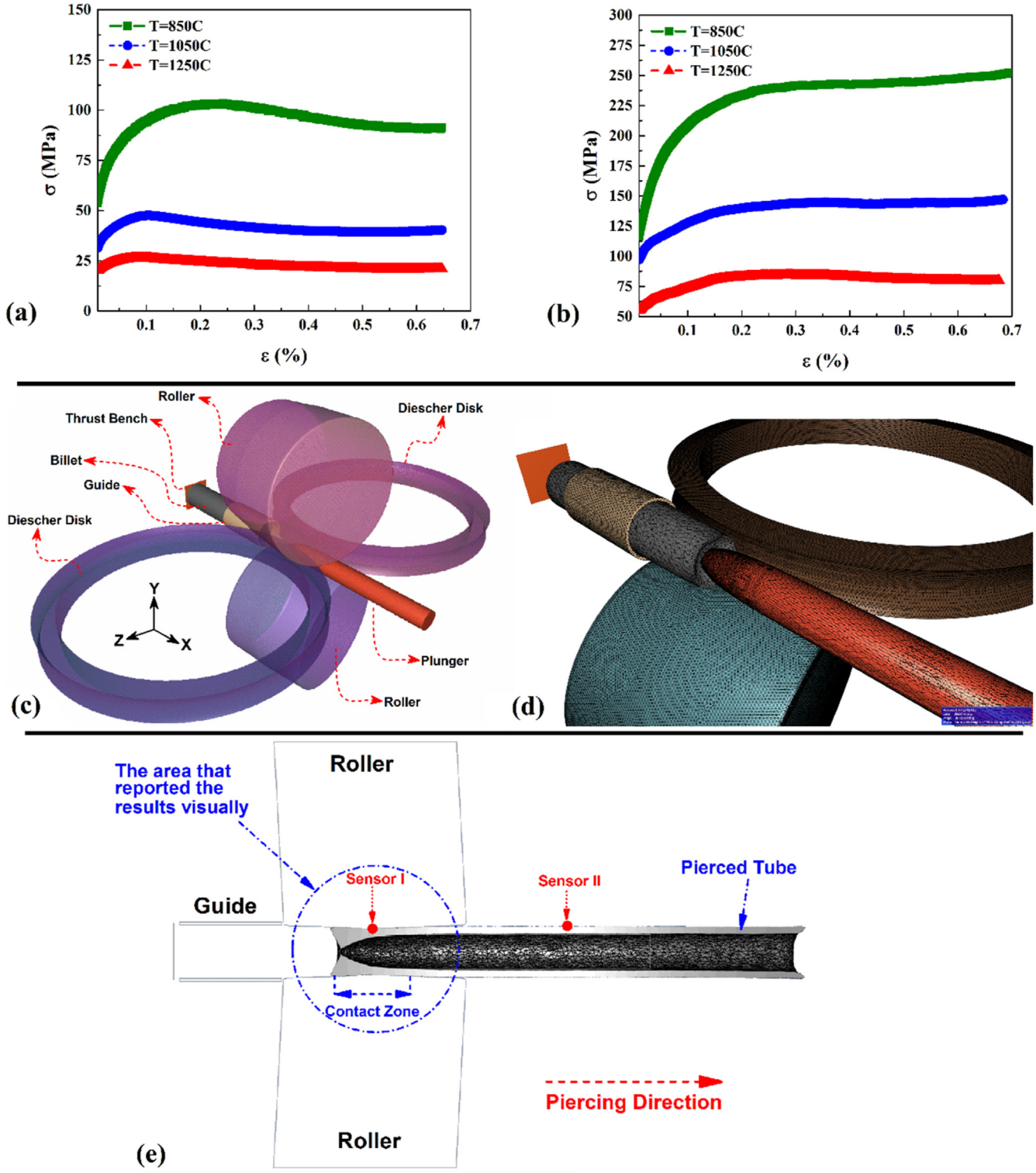

Fig. 3 – Super-martensitic Cr13 stainless steel flow-stress at (a) 0.01 s^{-1} and (b) 10 s^{-1} strain rates with various temperatures. (c) Schematic view of tool names. (d) Meshed parts in FORGE® NX. (e) The cross-section views of selected area for visualization report.

Table 2 – Friction parameters.

	Roller–Billet Interface	Plug–Billet Interface	Diescher -billet Interface
Friction Model	Viscoplastic	Tresca	Tresca
Friction Coefficient	0.1, 0.2, 0.3, 0.4, 0.5, 0.6	0.06, 0.1, 0.15	0.1

properties. The tools are meshed which different sizes and uniform mesh sets for billet. The rollers, Dieshers, plug, and guide were meshed by 2D triangular elements.

The billet meshed by 3D tetrahedral P1+ linear elements with a bubble node, size factor of 0.7, volumic size factor of 2.2, and minimum mesh size of 1.5 mm. The simulation domain, and the meshed components are presented in Fig. 3c and d, respectively. For better visualization, one Roller and one Diescher have been removed. Two sensors were put at the tip and middle of the tube during the simulation to collect the results after the simulation. After finish the simulation, the mean value results from sensors reported. For better visualization observation, the contact area at the end stage of the simulation is selected and presented. Fig. 3e presents a cross-section picture of the piercing process, sensors, contact zone, and visualization area.

4. Results and discussions

4.1. *Plastic deformation analysis*

Plastic deformation can be used to determine whether a tube is producible or not [21].

Plastic deformation is the permanent change in the shape of a raw material when subjected to a force or stress beyond its elastic limit. The total power during the skew rolling process consists of elastic power, plastic power and friction power. Plastic power is the rate of energy required to deform a material plastically. During the skew rolling process, plastic deformation occurs due to the application of heat and stress and the plastic power needed to deform the super-martensitic Cr13 stainless steel. In general, the plastic power of super-martensitic Cr13 stainless steel decreases due to the increased ductility at high temperatures compared with room-temperature plastic deformation. The required plastic power to deform the super-martensitic Cr13 stainless steel depends on various factors such as process temperature, process strain rate, and raw material properties. During the skew rolling process, the plastic power required to deform the metal depends on the material properties and the deformation conditions, and the plastic deformation that occurs is a result of the application of the necessary plastic power. In this research, the simulation results are validated by experimental data. A sample of pierced super-martensitic Cr13 stainless steel is presented in Fig. 4a. As mentioned, during the piercing process, the total power that leads to seamless tube formation is the sum of elastic power, plastic power, and friction power. An example of simulation results from power during the piercing process of RFC = 0.5 and PFC = 0.15 is depicted in Fig. 4b. All power components (Elastic, plastic, and friction powers) are linked with super-martensitic Cr13 stainless steel flow stress. The elastic power does not change dramatically by changing the friction. The plastic power is related to strain rate (which the friction power is not), but the plastic power is related to friction factor and tool speed (which the plastic power is not). The plastic power can effect on microstructural changes, and friction power can effect on frictional shear at the interface of materials and tools.

The effects of friction coefficient on power and energy are described in detail in a previous research of the authors [22]. For evaluation of various power calculated by FEM during the piercing process, the elastic, plastic, and friction power trends are presented in Fig. 4c–e, respectively. The trend shows that the elastic power increases from RFC = 0.01 to RFC = 0.5, and after that, it decreases slightly. The results revealed that the friction power has a sharp decrease from RPC = 0.1, and after that, it slightly increases after RFC = 0.5. The results of the plastic power of various samples (different RFC and PFC) are presented in Fig. 4d. According to the obtained results with increasing PFC, the plastic power increases in all samples. The increasing trend before RFC = 0.5 is more, and after RFC = 0.5, the plastic power trend is slightly moderated. It has been shown that plastic power increasing trend diminished due to the vast increase of frictional power in RFC of more than 0.5. The significant point in this result is that with increasing PFC, the progress in tube piercing debases and plastic deformation of super Cr 13 increases, and the plastic power increases [23].

4.2. *Thermal analysis*

The plastic deformation affects the temperature of super-martensitic Cr13 stainless steel during the piercing process. As mentioned before, the plastic power is the rate of energy required to deform super-martensitic Cr13 stainless steel with applied stress by the tooling system [24]. The changing friction coefficient at interfaces leads to changes on applied stress and plastic deformation on super-martensitic Cr13 stainless steel. The applied stress and plastic deformation can change the tube temperature during the piercing process. When a force is applied to a super-martensitic Cr13 stainless steel to cause it to deform (during the piercing process), the energy of the applied force is changed into strain energy. The strain energy is stored within the super-martensitic Cr13 stainless steel. However, not all this energy can be stored indefinitely, and some are converted into heat because the deformation process involves the movement of atoms [25]. The super-martensitic Cr13 stainless steel atom's movements generate frictional forces that convert mechanical energy into heat. The movements of atoms could be described with dislocation and microstructure analysis [25]. The analysis of temperature changes during the skew rolling process is essential for tooling system life, Control of forming process, properties of the tube after piercing, and quality control. The amount of heat generated after deformation can affect the material's microstructure, which in turn can affect the mechanical properties

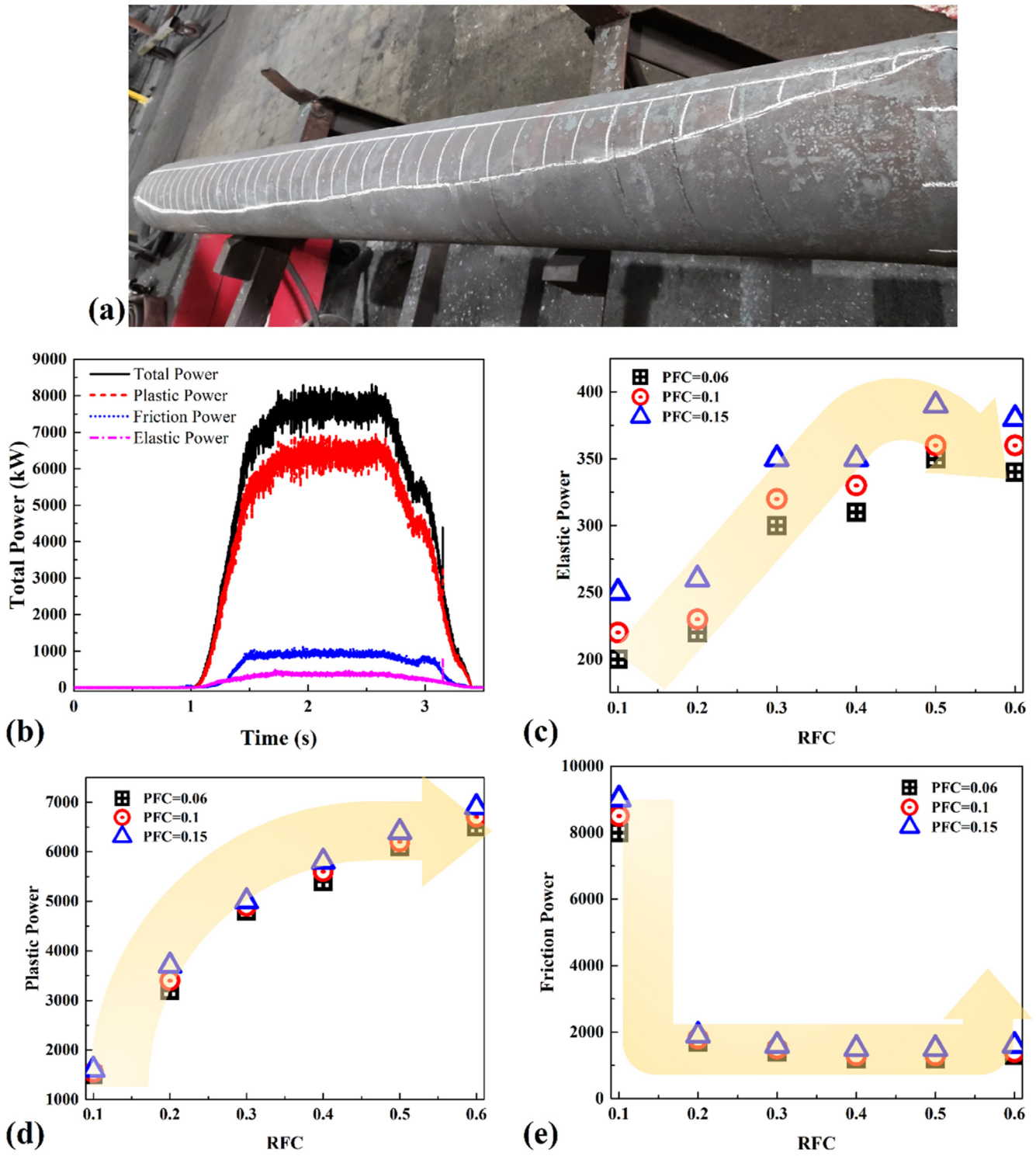

Fig. 4 – (a) A sample of pierced super-martensitic Cr13 stainless steel tube, (b) simulation results of elastic, friction, plastic and total power in case RFC = 0.5 and PFC = 0.15. The relation between RFC and PFC with (c) elastic power, (d) plastic power and (e) friction power.

of the finished product. The sufficient temperature during piercing can be adjusted to ensure that the super-martensitic Cr13 stainless steel remains ductile and can be shaped without fracturing at the tube's surface or along the tube's thickness. The relationship between plastic deformation and temperature in the skew rolling processes depends on several factors, such as billet microstructure, the rate of deformation, and the temperature of the billet at the piercing phase. In

general, increasing temperature during the skew rolling processes can increase the amount of plastic deformation the super-martensitic Cr13 stainless steel can undergo before it fails. For this reason, it is necessary to analyse the tube temperature evolution during piercing process and its relationship with deformation. A longitudinal-section view of temperature distribution in the pierced tube (RFC = 0.5 and PFC = 0.15) at the last step is presented in Fig. 5a. There it can be seen that the part of the tube that is starting the piercing is around 1100 °C, that is 150 °C cooler than the already pierced part. It means that the heat transfer of super-martensitic Cr13 stainless steel with air and tooling system decreases the temperature of super-martensitic Cr13 stainless steel near 150 °C form the 1250 °C which is the furnace set point temperature. After piercing, the temperature of raw material increases again up to the initial temperature. This phenomenon is related to plastic deformation. The temperature in the exterior and interior areas of the pierced tube uniformly increased. The surface temperature distribution of RFC = 0.1, 0.3, and 0.5 with PFC = 0.15 are presented in Fig. 5b–d, respectively. In the case of RFC = 0.1, the tube did not pierce, and the process was not finished. The reason was that the RFC could not push the hot metal forward and form the internal crack. Because the billet was heated previously, the super-martensitic Cr13 stainless steel was hot (around 1100 °C), and Rollers increased the temperature of the surface of the tube. In this case, the plastic deformation was not complete to pierce the tube, but local plastic deformation increased the heat locally. The results of case RFC = 0.1 is plotted at one step before the simulation stops—this plot aims to show how the temperature is distributing in failed samples. The RFC = 0.1 was unable to finish the process, but for friction values above RFC = 0.1, the piercing process was completed. As it can be seen, the tube temperature before contact with rollers and Diesher disks was near 1100 °C and then increased.

At the end of the tube, the temperature decreased again. This behavior is detectable for all samples. The comparison results between maximum temperature and friction coefficients are presented in Fig. 5e. Results show that the billet temperature increase occurred in all samples up to a range between 1200 °C and 1250 °C. The difference between low friction coefficient and high friction coefficient was not significant. Therefore, it can be concluded that the increasing temperature of the billet during forming is due to plastic deformation power, and the effect of friction is this regard is negligible. Higher plastic deformation led to higher plastic power leading to internal heat generation inside super-martensitic Cr13 stainless steel. The root of increasing temperature can be found in plastic deformation. The analysis of super-martensitic Cr13 stainless steel microstructure at various strain rates can help to describe plastic heating phenomena.

In subjecting plastic deformation, the temperature of the material increases due to the energy dissipation associated with the deformation process.

Microstructural changes do not directly cause an increase in temperature during plastic deformation, but they can indirectly influence the temperature through their effect on the deformation behavior of the super-martensitic Cr13 stainless steel [26]. Super-martensitic Cr13 stainless steel is categorized as high stacking fault material with many stacking faults within its crystal structure. This property can increase the probability of dislocation formation and accumulation, leading to a higher dislocation density. Higher dislocation density can increase the resistance of a material to deformation, which in turn can lead to a higher temperature during plastic deformation. This is because a greater force is required to deform the material, converting more energy into heat [27].

4.3. *Strain rate analysis*

The strain rate analysis during the piercing process gives information about the quality of the process and process time. The applied strain rate and its relationship with super-martensitic Cr13 stainless steel properties during the piercing process is considered in this section. During the piercing process, the maximum strain rate is applied to the tube at the interface of the tooling system. The Diescher disks have geometrical control roles, and Rollers do the push forwards. It can be concluded that the maximum strain rate is at the Roller-billet interface.

The contact area is where the Roller is in touch with the hot billet during the piercing process. A longitudinal-section view of the applied strain rate on the super-martensitic Cr13 stainless steel pierced by RFC = 0.5 and PFC = 0.15 are presented in Fig. 6a. The top view of this sample is presented in Fig. 6b. In the simulation process, the contact area between Roller and billet (which is depicted in Fig. 6b) consists of maximum strain rate area. The hot billet is tolerated this maximum strain sate from the piercing process until finishing.

As mentioned, after contacting hot billet the Rollers push it forward. At the early stage the contact area (which is consider as ¨ X˙ in Fig. 6c) is not complete. After the contact area increased by 50% (which is consider as ˙1.5 X˙ in Fig. 6d), the plug start to piercing (which is consider as˙P˙in Fig. 6d) and the Diescher disk control the geometry of piercing area (which is consider as˙D˙in Fig. 6d).

As mentioned, the results show that the strain rate is maximum at the areas of piercing and high deformation. In other words, the strain rate at the contact area of raw material with plug and Rollers is maximum. During the simulation, the friction model at the Roller-billet interface consider a viscoplastic model, and at Plug-billet, consider a Tresca model. In this situation, the rotational movement of the Rollers pushed the viscoplastic layer downward and forward. As mentioned, the plug does not have any movements (like an actual piercing process) and acts like a barrier for the internal shear layer. For this reason, the movement of the upper layer of the hot billet is more than the internal layer. A schematic view of piercing layers is presented in Fig. 6e. After piercing, the material does not handle any strain rate, because there is not any contact between tools and pierced tube. A sample of contact area and maximum strain rate from simulation results of PFC = 0.15 and RFC = 0.1, RFC = 0.3 and RFC = 0.5 are presented in Fig. 7a–c, respectively.

As it can be seen, the maximum strain rate is on the contact area between rollers and tube. A comparison between friction coefficient and maximum strain rate at contact area is

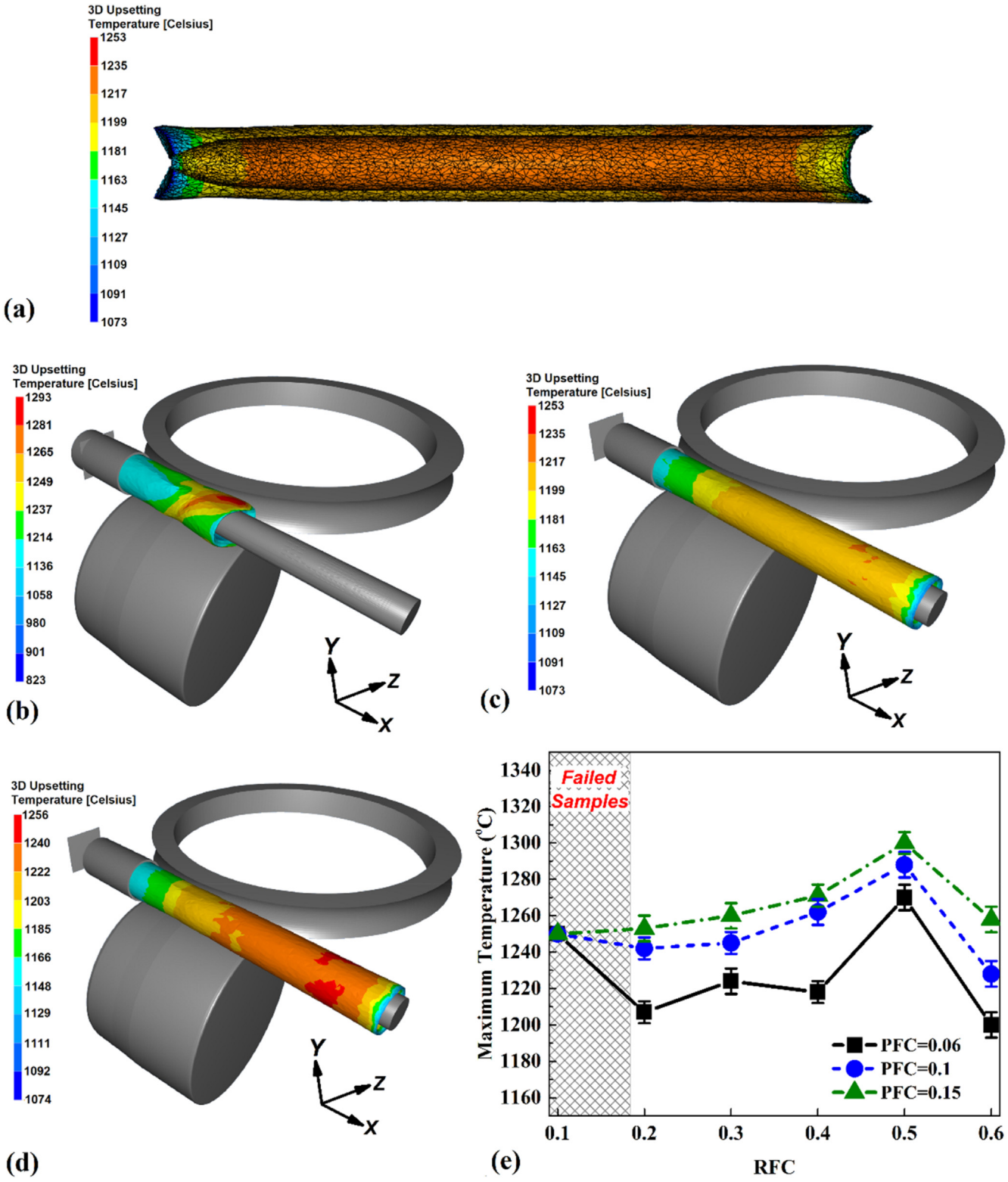

Fig. 5 – (a) Cross-section view of temperature distribution in tube that pierced by RFC = 0.5 and PFC = 0.15. Temperature distribution on the surface of tubes that pierced by PFC = 0.15 with (b) RFC = 0.1, (c) RFC = 0.3 and RFC = 0.5. (e) Comparisons between maximum temperature and friction coefficients.

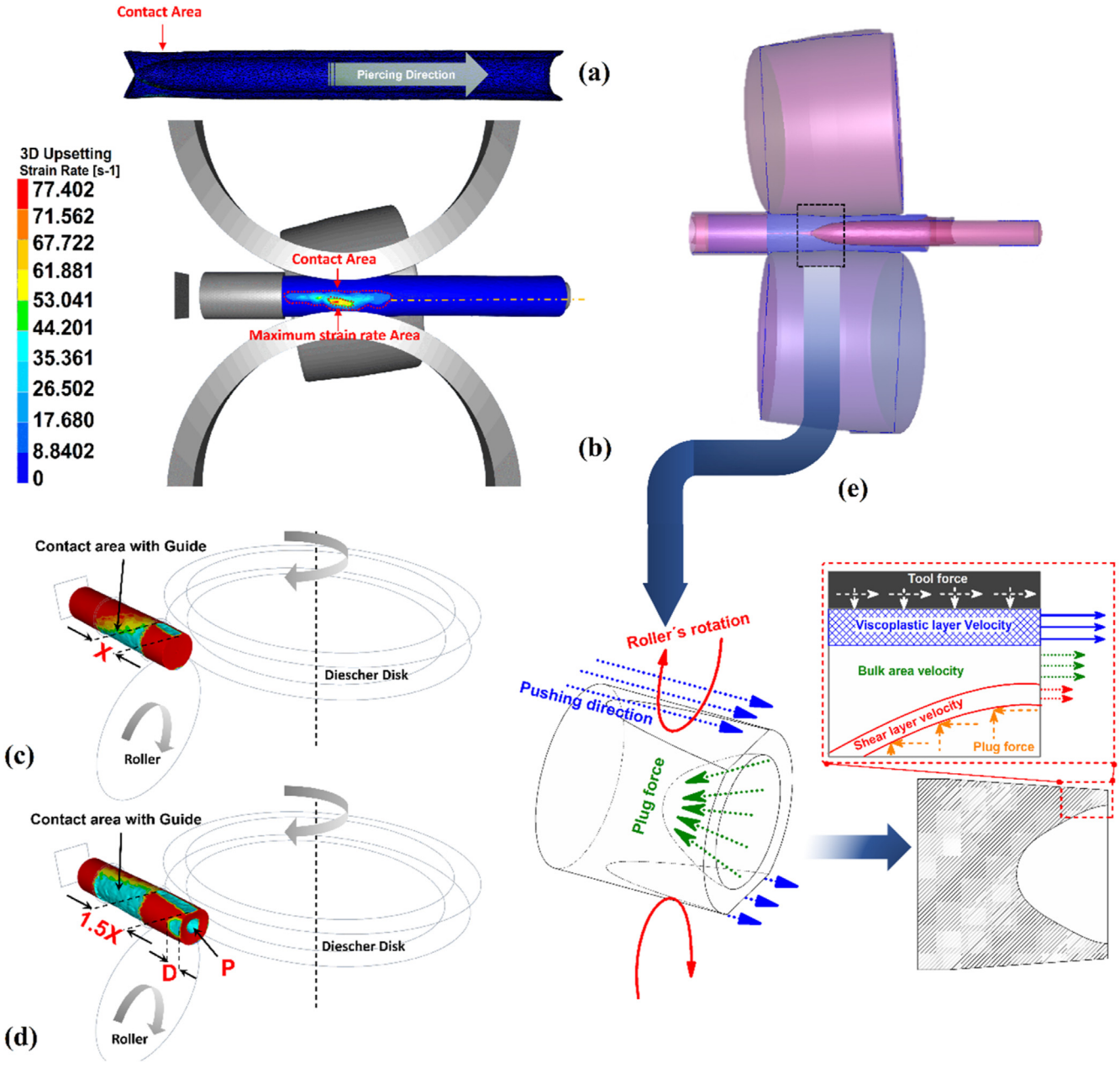

Fig. 6 – (a) Cross-section view of strain rate simulation in the tube that was pierced by RFC = 0.5 and PFC = 0.15. (b) Top view of contact area during simulation. Simulation results of (c) early stage Roller-billet contact and (d) Plug-billet contact. (e) Schematic view of viscoplastic and shear layer velocity directions.

presented in Fig. 7d. The results indicate that the strain rate increases with increasing RFC and decreases with increasing PFC. With increasing RFC, the rollers can push the super-martensitic Cr13 stainless steel forward faster, while increasing PFC acts like a barrier. The higher friction coefficient of the plug increases the processing time and the strain rate of forming process. Apart from RFC = 0.1 that tube piercing was not completed, the lowest value strain rate (~71 s^{-1}) was predicted in the piercing case with RFC = 0.2 and PFC = 0.15. The value of highest strain rate (~162 s^{-1}) that obtained in piercing case with RFC = 0.6 and PFC = 0.06.

The strain rate directly affects the phases and grain sizes of super-martensitic Cr13 stainless steel during and after the piercing process. Super-martensitic Cr13 stainless steel grain size refers to the size and arrangement of the grains within the microstructure. The microstructure of super-martensitic Cr13 stainless steel is composed of phases of martensite matrix, austenite, and δ-ferrite. The grain size of steel refers to the average dimension of these grains. The mentioned phases are formed during the piercing process, and after cooling down, their size may change due to static recrystallization phenomena.

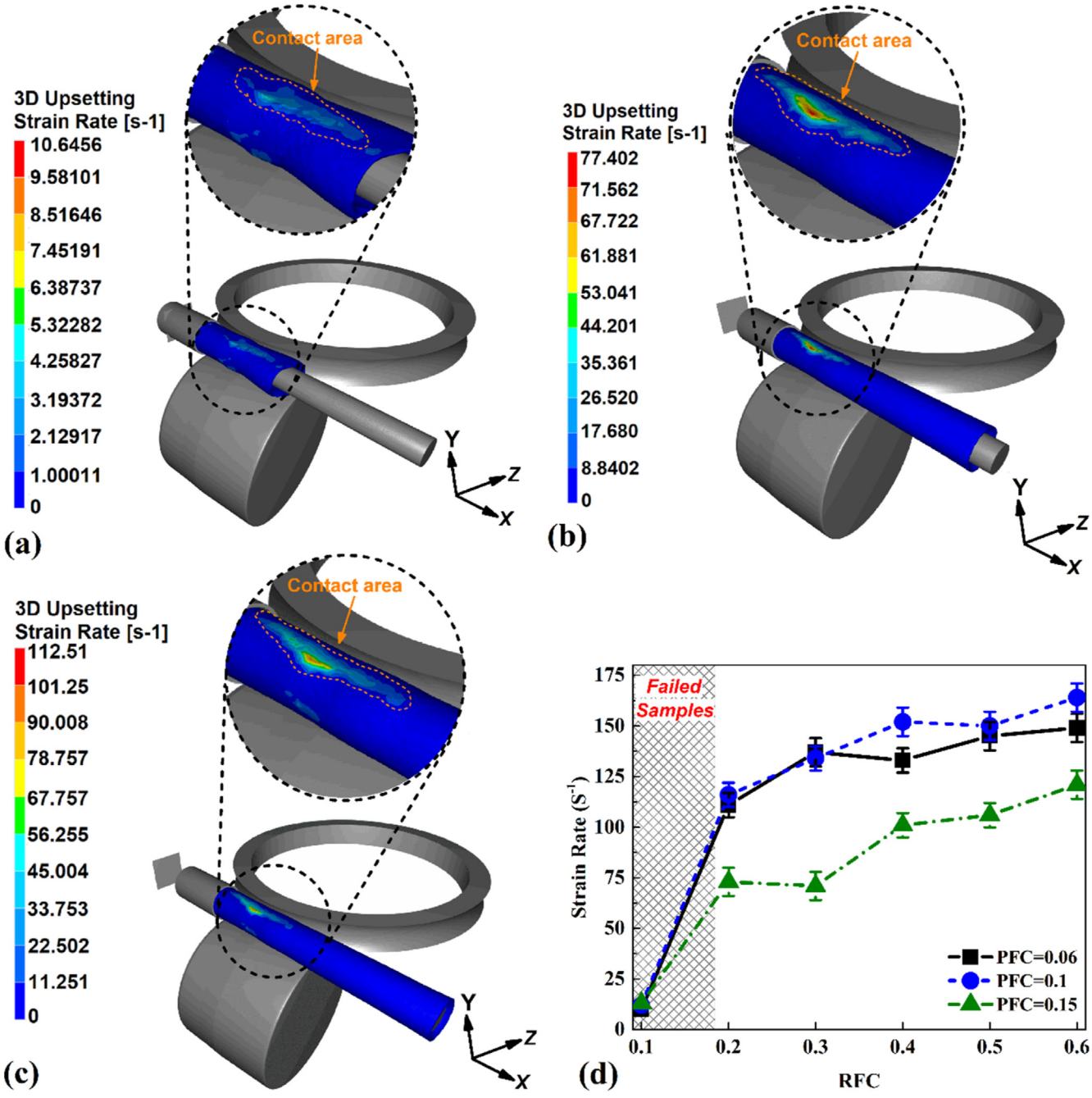

Fig. 7 – Strain rate on the surface of tubes that pierced by PFC = 0.15 with (a) RFC = 0.1, (b) RFC = 0.3 and (c) RFC = 0.5. (d) Comparisons between maximum strain rate and friction coefficients.

The histography of the microstructure of super-martensitic Cr13 stainless steel at 1100 °C at 10 s^{-1} and 0.01 s^{-1} is presented in Fig. 8a and b, respectively. As mentioned in the experimental section, the microstructure of the hot tensile sample was analyzed after the test and cooling down in cold water. The results indicate that the average grain size of super-martensitic Cr13 stainless steel was 7.8 μm and 9.0 μm for 10 s^{-1} and 0.01 s^{-1} strain rates, respectively. At higher strain rates, the grain size of super-martensitic Cr13 stainless steel decreases near 1.2 μm. There is an inverse relationship between average grain size and steel dislocation density [28]. When the grain size is small, there are more grain boundaries, and dislocations tend to accumulate at these boundaries, leading to a higher dislocation density. When the grain size is large, there are fewer grain boundaries, and dislocations tend to pile up and form larger cell structures within the grains [29].

More dislocations increase the energy required to deform the material, making it more difficult. For this reason, at higher RFC, the strain rate grows and increases the

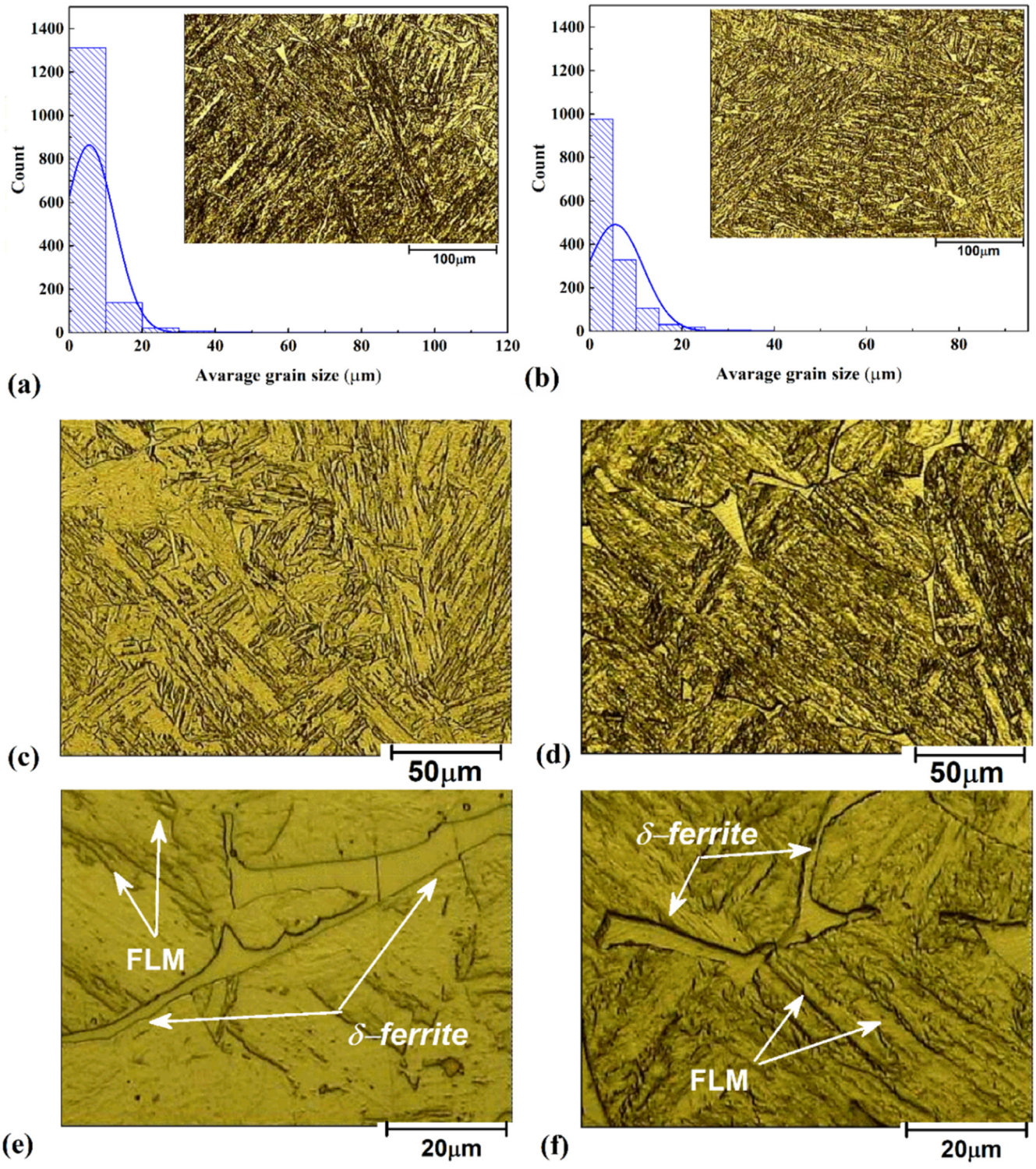

Fig. 8 – Histogram of microstructure of super-martensitic Cr13 stainless steel after (a) 10 s^{-1} and (b) 0.01 s^{-1} strain rate tensile test. Low magnification optical microscope image from microstructure of sample after (c) 10 s^{-1} and (d) 0.01 s^{-1} strain rate tensile test. High magnification optical microscope image from microstructure of sample after (e) 10 s^{-1} and (f) 0.01 s^{-1} strain rate tensile test.

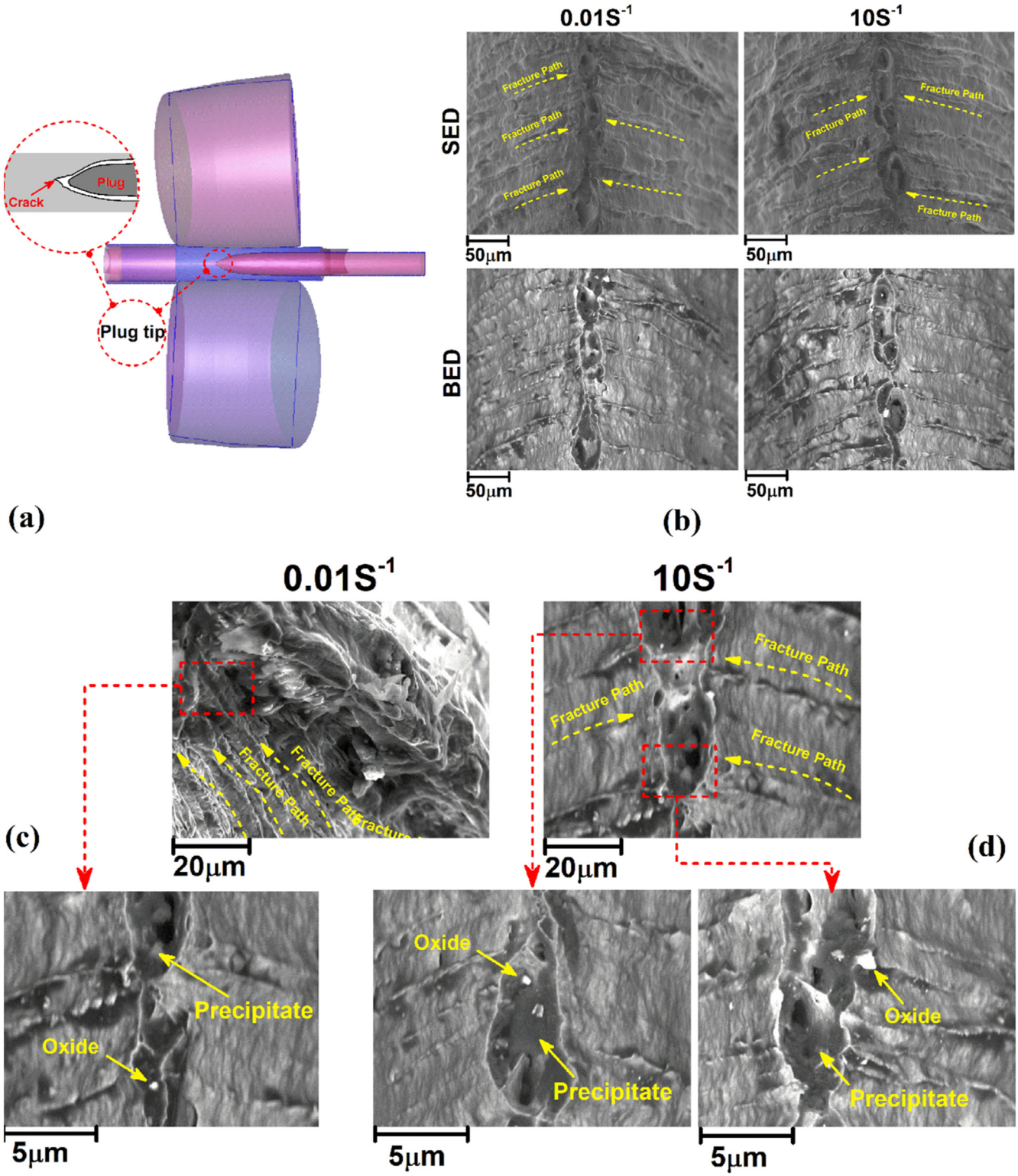

Fig. 9 – (a) Schematic view of plug tip cracks, (b) SE and BSE images from fracture surface of hot tensile test with 0.01 s^{-1} and 10 s^{-1} strain rate. High magnification BSE-SEM image from fracture surface of hot tensile test with (c) 0.01 s^{-1} and (d) 10 s^{-1}.

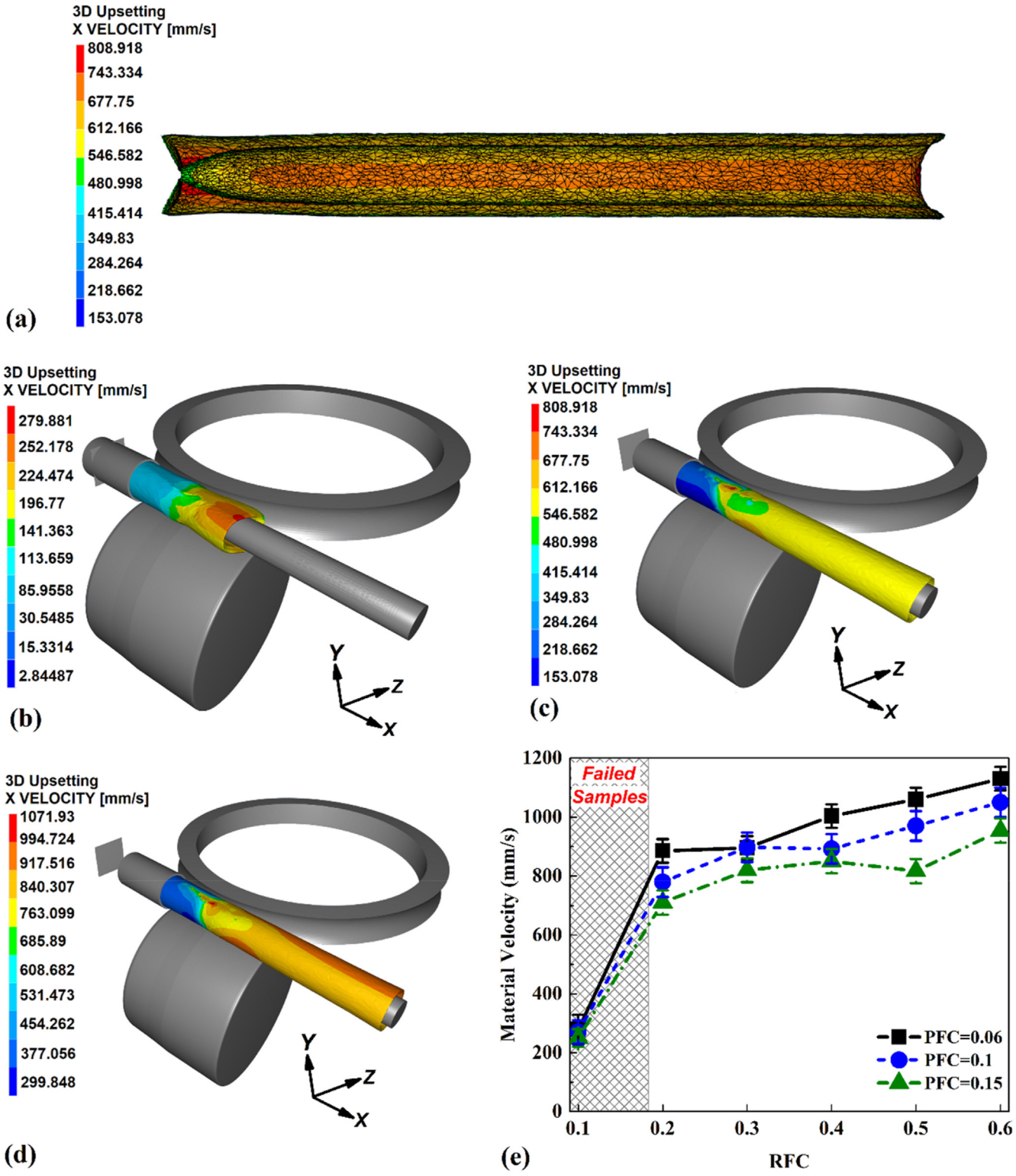

Fig. 10 – (a) Cross-section view of material velocity simulation in tube that pierced by RFC = 0.5 and PFC = 0.15. Strain rate on the surface of tubes that pierced by PFC = 0.15 with (b) RFC = 0.1, (c) RFC = 0.3 and RFC = 0.5. (e) Comparisons between maximum strain rate and friction coefficients.

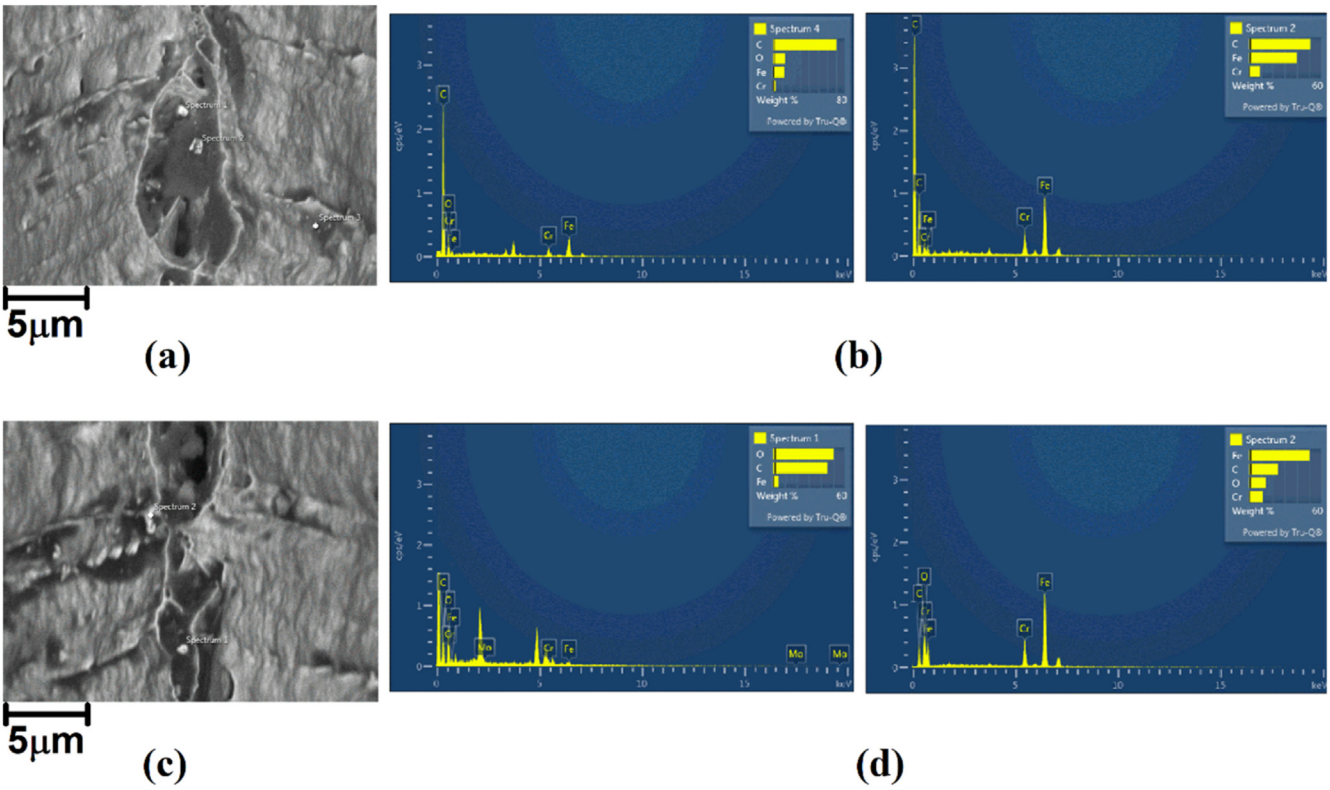

Fig. 11 – (a) BSE-SEM image of hot tensile test fracture surface after 0.01 s^{-1} strain rate and (b) EDS analysis from precipitates and oxide inside the fracture surface. (c) BSE-SEM image of hot tensile test fracture surface after 10 s^{-1} strain rate and (d) EDS analysis from precipitates and oxide inside the fracture surface.

temperature of the tube after the piercing process. The microstructure of super-martensitic Cr13 stainless steel, as a low carbon steel at testing temperatures between 950 °C and 1250 °C, is consists of γ-austenite (FCC structure) and δ-ferrite. After cooling to room temperature, martensite transformation leads to the formation of a full martensite matrix in the super-martensitic Cr13 stainless steel microstructure [30]. The low and high magnification of super-martensitic Cr13 stainless steel microstructure tensile samples tested at 10 s^{-1} and 0.01 s^{-1} are presented in Fig. 8c–f, respectively. The results revealed that the microstructure of super-martensitic Cr13 stainless steel in both cases almost consists of coarse lath martensite, fine lath martensite (FLM), and δ-ferrite.

During the piercing process, the plug pierced the hollow section of super-martensitic Cr13 stainless steel. The results indicate that the strain rate during the piercing process increases at higher RFC and lower PFC. This phenomenon is related to crack growth at the front of the plug. The schematic view of internal piercing and crack growth are presented in Fig. 9a. The SEM image analysis from the fracture surface of hot tensile tests with 0.01 s^{-1} and 10 s^{-1} strain rates are presented in Fig. 9b. The results consist of both secondary electron detector (SE) and the Backscattered electrons detector (BSE) results. The observation of the fracture surface analysis indicates that the fracture type in both cases was ductile. High-magnification BSE-SEM images from fractured surfaces are presented in Fig. 9c and d. Results show that the fracture surface at 0.01 s^{-1} strain rate consists of fine and coarse dimples, and the fracture surface at 10 s^{-1} strain rate primarily consists of coarse dimples. Coarse dimples indicate faster fracture growth during the hot-forming process. On the other hand, the fracture surfaces show oxide particles and precipitates trapped inside the dimples. The oxide particles have bright colors, and precipitates have a dark color. In order to understand and develop a better analysis regarding the chemical changes, BSE image was used. It seems that the strain rate of the tube during the piercing process affects the fracture type of super-martensitic Cr13 stainless steel and the chemical inactions. High friction coefficient leads to higher strain rates, and the internal fracture growth increases inside super-martensitic Cr13 stainless steel.

4.4. *Material velocity analysis*

The material velocity during the piercing process means how fast the hot cylinder can be pierced. This effect is related to the super-martensitic Cr13 stainless steel flowability, and the material velocity is directly related to process strain rate. The material velocity determines the processing time as well. A longitudinal-section view of material velocity on the super-martensitic Cr13 stainless steel that was pierced with RFC = 0.5 and PFC = 0.15 is presented in Fig. 10a. As it can be seen, the velocity contour

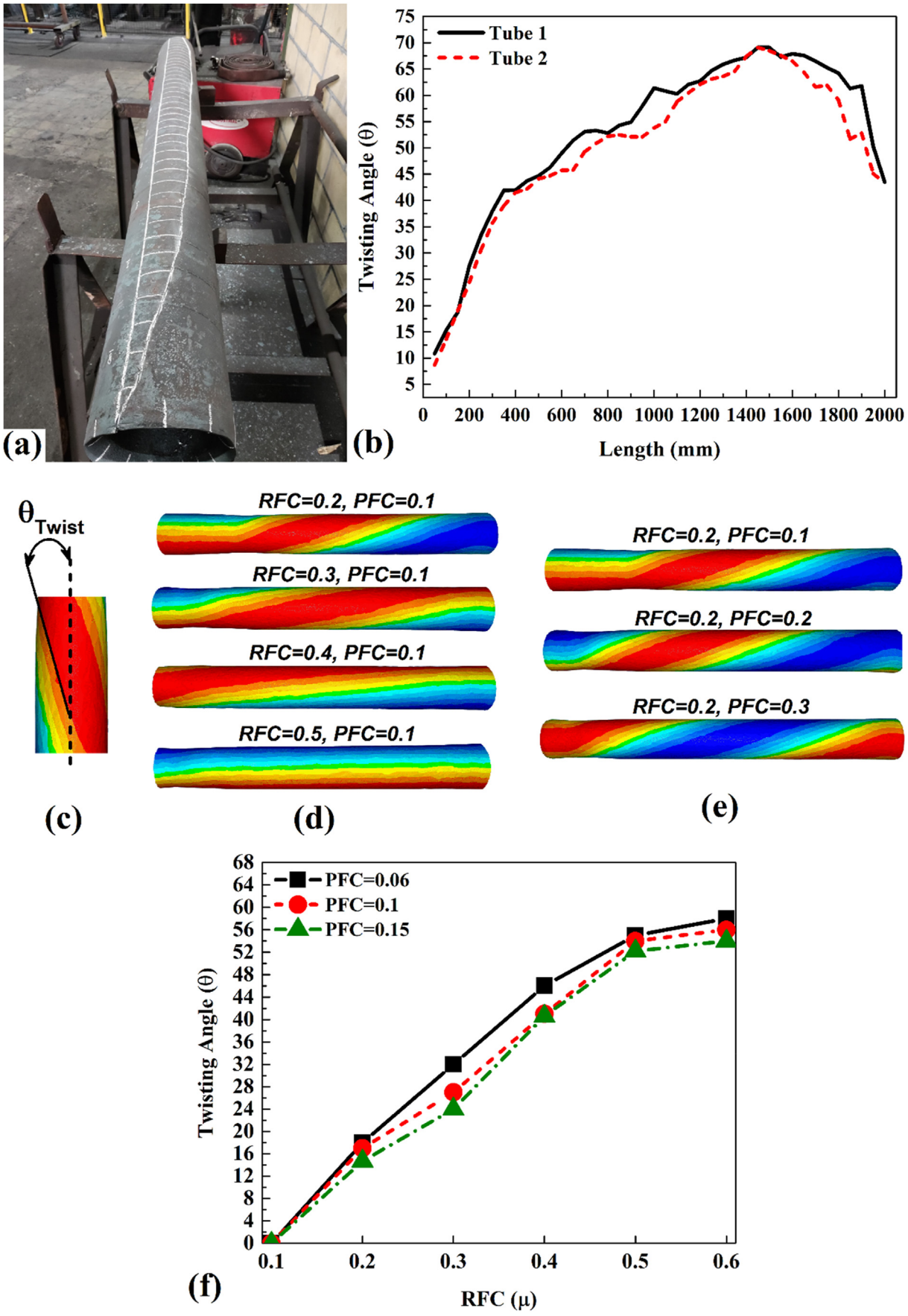

Fig. 12 – (a) Picture of twisted tube, (b) twisting angle along axis of pierced tubes. (c) Simulation results of twisting angle, simulation results of twisted angle at various (d) RFC and (e) PFC. (f) The maximum twisting angle of pierced tube at various friction coefficients.

indicates that the material velocity on the surface of the tube is higher than on the other areas. Due to the higher friction coefficient of RFC compared to PFC, the forward moving of raw material at the surface is faster than in the inside. The simulation results of material velocity at PFC = 0.15 and RFC = 0.1, RFC = 0.3, and RFC = 0.5 are presented in Fig. 10b–d, respectively. The material velocity at the contact area with the rollers increases dramatically because the rollers push it forward by friction and consequently the friction coefficient can affect the material velocity. The super-martensitic Cr13 stainless steel velocity after contact point with rollers became uniform. It means that the tube is uniformly formed.

As mentioned, the simulation results show that the maximum material velocity occurs at the roller's contact area. The relation between friction coefficient and material velocity is presented in Fig. 10e. The material velocity can be analyzed using the effects of PFC and RFC. Similar to the strain rate, increasing PFC decreases the material velocity. It means that a higher friction coefficient of the plug increases the piercing process time and tube formation. On the other hand, increasing RFC increases material velocity and decreases the piercing time by increasing material velocity. The simulation results revealed that the minimum material velocity was predicted at RFC = 0.2 and PFC = 0.15 (~650 mm/s), and the maximum velocity was at RFC = 0.6 and PFC = 0.06 (~1120 mm/s), respectively.

As discussed in microstructure analysis, the elongated δ-ferrite was observed in the tensile test with a 10 s^{-1} strain rate, while the shorter δ-ferrite existed in the tensile sample tested with 0.01 s^{-1}. From a metallurgical point of view, the δ-ferrite, which is formed at high temperatures, is the main reason for crack growth in low carbon Cr–Ni–Mo martensitic steels during high temperature forming process [31]. The δ-ferrite decrease the toughness of super-martensite steels at high temperature because of a lack of cohesion with the surrounding matrix [32]. At high temperatures and high strain rate, the Cr content near δ-ferrite reduces, due to precipitation of Cr-rich carbides (precipitates) in ferrite/martensite boundaries [33].

In general, the ferrite phase is weaker than other phases at high temperatures, and the presence of this phase increases the risk of hot rupture in super-martensitic steels [34]. The BSE-SEM image from the fracture surface of the hot tensile test at 0.01s^{-1} with the perspective of precipitation analysis is presented in Fig. 11a.

As it can be seen, dark points and shiny points are detected in dimples. The shiny points are iron oxides probably formed after the test when the sample's surface was hot and hot iron elements reacted with environment oxygen. Due to the rapid cooling of the hot tensile sample, this oxide is not much on the fracture surface. On the other hand, the dark point indicates the carbides precipitates. A sample of EDS point analysis from these points is presented in Fig. 11b. The results indicate that the chemical composition of these precipitates is $Cr_{23}C_6$, a common carbide precipitate in high chromium steels. The BSE-SEM image from the fracture surface of the hot tensile test after 10 s^{-1} is presented in Fig. 11c. A sample of EDS point analysis from precipitates is presented in Fig. 10d. The results show that the bigger precipitates are formed in the 10 s^{-1} sample. This result confirms that at a high strain rate and high temperature precipitates are formed in the super-martensite matrix, and δ-ferrite leads to crack initiation and growth. The higher RFC increases the piercing process strain rate, and the higher PFC decreases the strain rate. Increasing the strain rate helps in the formation of longer δ-ferrite inside the hot billet and increases the fracture growth inside the piercing tube. These effects help to increase material velocity and thus lower the process time.

4.5. *Tube twisting analysis*

During the seamless tube piercing process, surface twisting can occur if the tooling system and the billet material are not correctly aligned or if the billet material is not uniformly deformed. Surface twisting is also known as a defect that can lead to a non-uniform wall thickness. Twisting is a surface phenomenon related to the strain rate and material velocity. The tooling system interface's friction coefficient can change super-martensitic Cr13 stainless steel's deformation and consequently lead to tube twisting changes. A sample of the pierced tube with the surface mark is depicted in Fig. 12a. For this measurement, 25 points were marked on raw billet, and after the piercing process, the placement changes of the point at the surface of the tube were investigated. For this purpose, the displacement points connect and make a curve on the surface of the tube. Then the curve angle with the longitudinal axis of the tube was calculated, and the twisting angle was presented [35]. In this regard, twisting angles from top to bottom of the tube surface were calculated, and the results are presented in Fig. 12b. The results show that the twisting angle at middle is maximum and at tip of is minimum. Consequently, in the simulation the twisting at the center of the tube (Fig. 12c) is considered. The surface tube twisting at various RFC and PFC are presented in Fig. 12d and e, respectively. The maximum surface twisting angle of tubes pierced with different friction coefficients is presented in Fig. 11f. The results indicate that with increasing RFC, the twisting angle increase, and with increasing PFC, the twisting angle decreases.

This behavior is expected because with increasing RFC and decreasing PFC, the strain rate of the deformation process increases. The experimental results show that the maximum twisting angle was 69.1°. The simulation results indicated that the maximum twisting was on RFC = 0.6 and PFC = 0.06 (~58°), while the minimum twisting angle was formed on the tube pierced by RFC = 0.2 and PFC = 0.15 (~13°).

5. Conclusion

In this article, the skew rolling piercing process is modeled by the finite element method in three dimensions. The effects of friction coefficients on the material velocity, strain rate, and thermal properties were analyzed during the process. Experimental data validated the simulation results. The materials' behavior during the piercing process was analyzed, and

compared to the results of hot tensile material characterization tests. The conclusions are presented below:

1 The plastic deformation power is increased by increasing RFC and decreasing by PFC. The increasing plastic deformation at higher RFC increased the temperature of the super-martensitic Cr13 stainless steel tube after piercing around 100 °C. The tube in RFC = 0.1 was non-producible, and the maximum plastic power was at RFC = 0.5 and PFC = 0.15.
2 The maximum strain rate predicted at RFC = 0.5 and PFC = 0.06 (162 s^{-1}) was 225% more than the minimum strain rate (72s^{-1}) produced at RFC = 0.2 and PFC = 0.15. The higher strain rate leads to rapid ductile fracture at high temperatures with the benefit of faster piercing during skew rolling of super super-martensitic Cr13 stainless steel.
3 The maximum material velocity (~1120 mm/s) was 172% more than the minimum material velocity (~650 mm/s). The material velocity is result of strain rate and internal crack growth during skew rolling. Higher RFC leads to higher material velocity during the piercing process, and higher PFC decreases the material velocity. The microstructural changes and formation of precipitates during piercing process is effects the super-martensitic Cr13 stainless steel velocity during piercing process.
4 The RFC has significant effects on tube twisting during piercing process. The higher RFC leads to more surface twisting angles. The maximum surface twisting angle produced at RFC = 0.6, PFC = 0.06 (58°), and the minimum twisting angle produced at RFC = 0.2, PFC = 0.15 (13°).

Declaration of Competing Interest

The authors declare that they have no known competing financial interests or personal relationships that could have appeared to influence the work reported in this paper.

Acknowledgments

This project has received funding from the European Union's Horizon 2020 Research and Innovation Programme under the Marie Skłodowska-Curie grant agreement No. 847624. In addition, a number of institutions back and co-finance this project. The paper reflects only the authors' view and the Agency is not responsible for any use that may be made of the information it contains.

REFERENCES

[1] Skripalenko MM, Karpov BV, Rogachev SO, Kaputkina LM, Romantsev BA, Skripalenko MN, et al. Simulation of the kinematic condition of radial shear rolling and estimation of its influence on a titanium billet microstructure. Materials (Basel). 2022;15:7980. https://doi.org/10.3390/ma15227980.
[2] Galkin SP, Gamin YV, Kin TY. Analysis of temperature influence on strain–speed parameters of radial-shear rolling of Al-Zn-Mg-Ni-Fe alloy. Materials (Basel). 2022;15:7202. https://doi.org/10.3390/ma15207202.
[3] Xia Y, Shu X, Shi J, Wang Y, Pater Z, Wang J. Forming quality research on the variable-diameter section of the hollow axle in three-roll skew rolling. Materials (Basel). 2022;15:5614. https://doi.org/10.3390/ma15165614.
[4] Pater Z, Wójcik Ł, Walczuk P. Comparative analysis of tube piercing processes in the two-roll and three-roll mills. Adv Sci Technol Res J 2019;13:37–45. https://doi.org/10.12913/22998624/102766.
[5] Ding X, Kuai Y, Li T, Zhou Y, Shuang Y. Enhanced mechanical properties of magnesium alloy seamless tube by three-roll rotary piercing with severe plastic deformation. Mater Lett 2022;313:131655. https://doi.org/10.1016/j.matlet.2022.131655.
[6] Topa A, Cerik BC, Kim DK. A useful manufacturing guide for rotary piercing seamless pipe by ALE method. J Mar Sci Eng 2020;8:756. https://doi.org/10.3390/jmse8100756.
[7] Urbanski S, Kazanecki J. Assessment of the strain distribution in the rotary piercing process by the finite element method. J Mater Process Technol 1994;45:335–40. https://doi.org/10.1016/0924-0136(94)90362-X.
[8] Mori K, Yoshimura H, Osakada K. Simplified three-dimensional simulation of rotary piercing of seamless pipe by rigid–plastic finite-element method. J Mater Process Technol 1998;80–81:700–6. https://doi.org/10.1016/S0924-0136(98)00128-9.
[9] Topa A, Kim DK, Kim Y. 3D numerical simulation of seamless pipe piercing process by fluid-structure interaction method. MATEC Web Conf 2018;203. https://doi.org/10.1051/matecconf/201820306016.
[10] Ceretti Elizabeth, Gardens Claudio, Attanasio A. Analysis of rotary tube piercing process: simulation and experimental results. Proc AITEM 2001;1:1.
[11] Pietsch J, Thieven P. FEM simulation of the rotary tube piercing process. MPT Int 2003;2:25–60.
[12] Ceretti E, Giadini C, Attanasio A, Brisotto F, Capoferri G. Rotary tube piercing study by FEM analysis: 3D simulations and experimental results. Tube Pipe Technol 2004:155–9.
[13] Berazategui DA, Cavaliere MA, Montelatici L, Dvorkin EN. On the modelling of complex 3D bulk metal forming processes via the pseudo-concentrations technique. Application to the simulation of the Mannesmann piercing process. Int J Numer Methods Eng 2006;65:1113–44. https://doi.org/10.1002/nme.1475.
[14] Pater Z, Kazanecki J, Bartnicki J. Three dimensional thermo-mechanical simulation of the tube forming process in Diescher's mill. J Mater Process Technol 2006;177:167–70. https://doi.org/10.1016/j.jmatprotec.2006.03.205.
[15] Pater Z, Kazanecki J. Thermo-mechanical analysis of piercing plug loads in the skew rolling process of thick-walled tube shell. Metall Foundry Eng 2006;32:31. https://doi.org/10.7494/mafe.2006.32.1.31.
[16] Zhao YQ, Mao JH, Liu FF, Ma ZH. Experiments and simulation on mannesmann piercing process in the drill steel manufacture. Strength Mater 2015;47:29–40. https://doi.org/10.1007/s11223-015-9624-4.
[17] Murillo-Marrodán A, Garcia E, Cortés F. Friction modelling of a hot rolling process by means of the finite element method. 2017. London.
[18] Fernandes M, Marouf N, Montmitonnet P, Mocellin K. Impact of the different friction coefficients on the tools on the mechanics of the mannesmann 2-roll tube piercing. ISIJ Int 2020;60:2917–26. https://doi.org/10.2355/isijinternational.ISIJINT-2020-290.

[19] Aghajani Derazkola H, Garcia E, Murillo-Marrodán A. Effects of tool–workpiece interfaces friction coefficient on power and energy consumption during the piercing phase of seamless tube production. J Mater Res Technol 2022;19:3172–88. https://doi.org/10.1016/j.jmrt.2022.06.071.
[20] No Title Available online: https://www.tubosreunidosgroup.com/en/home.
[21] Cao X, Wang B, Zhou J, Shen J. Application of unified constitutive model of 34CrNiMo6 alloy steel and microstructure simulation for flexible skew rolling hollow shafts. J Manuf Process 2022;76:598–610. https://doi.org/10.1016/j.jmapro.2022.02.021.
[22] Aghajani Derazkola H, Garcia E, Murillo-Marrodán A. Effects of tool-workpiece friction condition on energy consumption during piercing phase of seamless tube production. Key Eng Mater 2022;926:602–11. https://doi.org/10.4028/p-70x28i.
[23] Zhang D-W, Li D-H, Liu B-K, Yu Z-C, Zhao S-D. Investigation and implementation for forming lead screw by through-feed rolling process with active rotation. J Manuf Process 2022;82:96–112. https://doi.org/10.1016/j.jmapro.2022.07.062.
[24] Pater Z, Tomczak J, Bulzak T, Li Z. Analysis of the use of variable angular parameter tools in cross-wedge rolling. J Manuf Process 2022;83:768–86. https://doi.org/10.1016/j.jmapro.2022.09.052.
[25] Jo SY, Hong S, Han HN, Lee M-G, Cao H, Chen W. Modeling and simulation of steel rolling with microstructure evolution: an overview. Steel Res Int 2023;94:2200260. https://doi.org/10.1002/srin.202200260.
[26] Derazkola HA, Gil EG, Murillo-Marrodán A, Méresse D. Review on dynamic recrystallization of martensitic stainless steels during hot deformation: Part i—experimental study. Metals 2021:11.
[27] Aghajani Derazkola H, Garcia E, Murillo-Marrodán A, Conde Fernandez A. Review on modeling and simulation of dynamic recrystallization of martensitic stainless steels during bulk hot deformation. J Mater Res Technol 2022;18:2993–3025. https://doi.org/10.1016/j.jmrt.2022.03.179.
[28] Avendaño-Rodríguez DF, Rodriguez-Baracaldo R, Weber S, Mujica-Roncery L. Damage evolution and microstructural fracture mechanisms related to volume fraction and martensite distribution on dual-phase steels. Steel Res Int 2023:2200460. https://doi.org/10.1002/srin.202200460. *n/a*.
[29] Wei H, Deng X, Chen S, Zhou Z, Pan H. Study on hot flow behaviors and deformation/diffusion mechanisms of V and V–Ti microalloyed steels by physical constitutive modeling. Steel Res Int 2023:2200847. https://doi.org/10.1002/srin.202200847. n/a.
[30] Eres-Castellanos A, Garcia-Mateo C, Caballero FG. Future trends on displacive stress and strain induced transformations in steels. Metals 2021;11:299. https://doi.org/10.3390/met11020299.
[31] Wei YL. Microstructural characterization and mechanical properties of super 13＼% Cr steel. 2005.
[32] Bashu SA, Singh K, Rawat MS. Effect of heat treatment on mechanical properties and fracture behaviour of a 12CrMoV steel. Mater Sci Eng A 1990;127:7–15. https://doi.org/10.1016/0921-5093(90)90184-5.
[33] Hara T, Asahi H. Effect of d d-ferrite on sulfide stress cracking in a low carbon 13 mass% chromium steel. ISIJ Int 2000;40:1134–41. https://doi.org/10.2355/isijinternational.40.1134.
[34] Derazkola HA, Garcia E, Murillo-Marrodán A, Hardell J. The effect of temperature and strain rate on the mechanical properties and microstructure of super Cr13 martensitic stainless steel. J Mater Res Technol 2023;24:3464–76. https://doi.org/10.1016/j.jmrt.2023.04.012.
[35] Murillo-Marrodán A, García E, Barco J, Cortés F. Analysis of wall thickness eccentricity in the rotary tube piercing process using a strain correlated FE model. Metals 2020;10:1–18.